

# Carrier dynamics and coherent acoustic phonons in nitride heterostructures

G. D. Sanders and C. J. Stanton

Department of Physics, University of Florida, Box 118440  
Gainesville, Florida 32611-8440

(Dated: July 2, 2018)

We model generation and propagation of coherent acoustic phonons in piezoelectric InGaN/GaN multi-quantum wells embedded in a *pin* diode structure and compute the time resolved reflectivity signal in simulated pump-probe experiments. Carriers are created in the InGaN wells by ultrafast pumping below the GaN band gap and the dynamics of the photoexcited carriers is treated in a Boltzmann equation framework. Coherent acoustic phonons are generated in the quantum well via both deformation potential electron-phonon and piezoelectric electron-phonon interaction with photogenerated carriers, with the latter mechanism being the dominant one. Coherent longitudinal acoustic phonons propagate into the structure at the sound speed modifying the optical properties and giving rise to a giant oscillatory differential reflectivity signal. We demonstrate that coherent optical control of the differential reflectivity can be achieved using a delayed control pulse.

PACS numbers: 63.20.Kr, 63.22.+m, 78.20.Hp, 78.47.+p

## I. INTRODUCTION

Femtosecond transient reflectivity spectroscopy has proven useful in the study of carrier dynamics in bulk semiconductors and semiconductor heterostructures as well as the study of the generation and propagation of coherent phonons in a number of materials. In particular, coherent optical phonons have been observed in bulk semiconductors<sup>1,2</sup> and coherent acoustic phonons have been detected in InGaN/GaN-based semiconductor heterostructures.<sup>3,4,5,6,7,8</sup>

We recently developed a detailed theory for carrier dynamics and time resolved differential reflectivity in two-color pump-probe experiments on nonpiezoelectric  $\text{In}_x\text{Mn}_{1-x}\text{As}/\text{GaSb}$  heterostructures, which agreed well with experimental measurements.<sup>9,10</sup> Oscillations were observed in the differential reflectivity which we attributed to the generation and propagation of coherent acoustic phonon wave packets, which altered the local dielectric function as they propagated through the structure at the LA phonon sound speed. The carrier dynamics in the two-color pump-probe experiments were modeled using a Boltzmann equation formalism including photogeneration of carriers by the pump laser and their subsequent cooling and relaxation by emission of confined LO phonons. The recombination of electron-hole pairs via the Shockley-Read carrier trapping mechanism was included in a simple relaxation time approximation.

The differential reflectivity was obtained by solving Maxwell's equations throughout the structure using a transfer matrix method. In addition to the coherent phonon induced reflectivity oscillations, a strong background signal was observed which we attributed to: (1) enhanced Drude absorption by photoexcited carriers, (2) relaxation dynamics due to cooling of hot photoexcited carriers by LO phonon scattering, and (3) nonradiative recombination of electron-hole pairs at midgap defects.

A microscopic theory for the generation and propagation of coherent acoustic phonons in piezoelectric wurtzite

semiconductors was developed in Ref. 11 (see the erratum in Ref. 12 and the review article by Chern *et al* in Ref. 3). It was found that generation of coherent acoustic phonons by means of photoexcited carriers occurs through the deformation potential electron-phonon interaction and the piezoelectric electron-phonon interaction, with the latter typically being an order of magnitude stronger. While the work of Ref. 11 concerned itself with the generation and propagation of coherent acoustic phonons in piezoelectric heterostructures, it did not address the question of their detection in time resolved differential reflectivity experiments.

Our earlier paper (Ref. 9) described the generation and propagation of coherent acoustic phonons in Zinc Blende semiconductor heterostructures in which the generation of coherent acoustic phonons can only occur by means of the weaker deformation potential electron-phonon mechanism. In this paper we are motivated to extend the results of Ref. 9 to piezoelectric wurtzite heterostructures where the coherent phonon induced differential reflectivity oscillations are expected to be much stronger.

## II. THEORY

We model photogeneration of electrons and holes and the subsequent excitation of coherent acoustic phonons in a nitride based multi-quantum well (MQW) *pin* diode shown schematically in Fig. 1. Such a nitride structures have been used in recent experimental studies by Y. D. Jho *et al* in Refs. 13 and 14. The structures are grown on an undoped 1.5  $\mu\text{m}$  thick GaN layer grown on top of an  $a_c$ -plane sapphire substrate and we base our theoretical studies on a similar structure. The intrinsic region of the diode is an undoped MQW heterostructure consisting of five 22  $\text{\AA}$   $\text{In}_{0.15}\text{Ga}_{0.85}\text{N}$  wells separated by 100  $\text{\AA}$  GaN barriers. The growth direction is along (0001). The multi-quantum well structure is the intrinsic region of a *pin* diode with contacts consisting of p- and n-doped

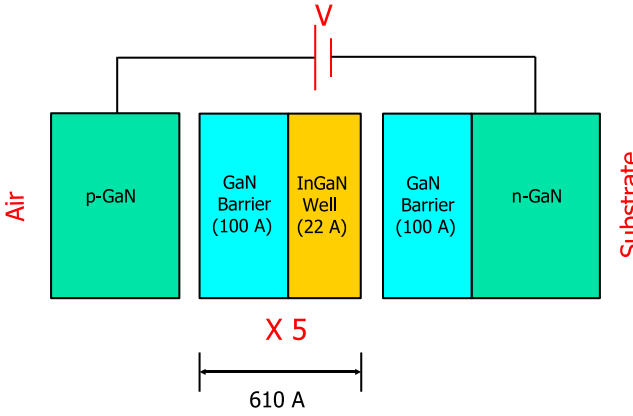


FIG. 1: Schematic diagram of the multi-quantum well *pin* diode structure.

GaN substrate and cap layers. The thickness of the n-GaN cap layer is taken to be 100 Å, which is thinner than that used in Refs. 13 and 14, and the width of the intrinsic region  $L$  is 710 Å as can be seen in Fig. 1. The voltage drop across the intrinsic region is  $\Delta V$ . For the structure described in Refs. 13 and 14 the voltage drop across the intrinsic region is  $\Delta V \approx 1.6$  volts when the external voltage across the diode is  $V = 0$  volts and we adopt this value in our studies.

### A. Bulk Bandstructure

Our first task is to model the electronic states in the device shown in Fig. 1. In bulk systems, the conduction and valence bands in wurzite crystals including the effects of strain are treated using effective mass theory. Near the band edge, the effective mass Hamiltonian for electrons is described by a  $2 \times 2$  matrix which depends explicitly on electron wavevector,  $\mathbf{k}$ , and the strain tensor,  $\epsilon$ . The electron Bloch basis states are

$$|c, 1\rangle = |S \uparrow\rangle \quad (1a)$$

$$|c, 2\rangle = |S \downarrow\rangle. \quad (1b)$$

The conduction band effective mass Hamiltonian is diagonal and is given by (relative to the bottom of the conduction band) (Refs. 15 and 16)

$$H_{2 \times 2}^c(\mathbf{k}, \epsilon) = \left\{ \frac{\hbar^2 k_z^2}{2m_z^*} + \frac{\hbar^2 k_t^2}{2m_{xy}^*} + a_{c,z} \epsilon_{zz} + a_{c,xy} (\epsilon_{xx} + \epsilon_{yy}) \right\} \mathbf{I}_{2 \times 2}. \quad (2)$$

where  $\mathbf{I}_{2 \times 2}$  is the identity matrix. The electron effective masses along  $z$  (taken parallel to the c-axis) and in the  $xy$  plane are  $m_z^*$  and  $m_{xy}^*$ , respectively,  $k_t^2 = k_x^2 + k_y^2$ , and  $\epsilon_{xx}$ ,  $\epsilon_{yy}$  and  $\epsilon_{zz}$  are strain tensor components, and  $a_{c,z}$  and  $a_{c,xy}$  are the deformation potentials.

The Hamiltonian for the valence bands is a  $6 \times 6$  matrix. Following Ref. 17, the Hamiltonian (relative to the top of the valence band) can be block diagonalized into two degenerate  $3 \times 3$  submatrices if we adopt the Bloch basis states

$$|v, 1\rangle = -\frac{\alpha^*}{\sqrt{2}} |(X + iY) \uparrow\rangle + \frac{\alpha}{\sqrt{2}} |(X - iY) \downarrow\rangle \quad (3a)$$

$$|v, 2\rangle = \frac{\beta}{\sqrt{2}} |(X - iY) \uparrow\rangle - \frac{\beta^*}{\sqrt{2}} |(X + iY) \downarrow\rangle \quad (3b)$$

$$|v, 3\rangle = \beta^* |Z \uparrow\rangle + \beta |Z \downarrow\rangle \quad (3c)$$

$$|v, 4\rangle = -\frac{\alpha^*}{\sqrt{2}} |(X + iY) \uparrow\rangle - \frac{\alpha}{\sqrt{2}} |(X - iY) \downarrow\rangle \quad (3d)$$

$$|v, 5\rangle = \frac{\beta}{\sqrt{2}} |(X - iY) \uparrow\rangle + \frac{\beta^*}{\sqrt{2}} |(X + iY) \downarrow\rangle \quad (3e)$$

$$|v, 6\rangle = -\beta^* |Z \uparrow\rangle + \beta |Z \downarrow\rangle. \quad (3f)$$

The phase factors,  $\alpha$  and  $\beta$ , are functions of the angle  $\phi = \tan^{-1}(k_y/k_x)$  and are given by

$$\alpha(\phi) = \frac{1}{\sqrt{2}} e^{i(3\pi/4 + 3\phi/2)} \quad (4a)$$

$$\beta(\phi) = \frac{1}{\sqrt{2}} e^{i(\pi/4 + \phi/2)}. \quad (4b)$$

The block diagonalized Hamiltonian can be written as

$$H_{6 \times 6}^v(\mathbf{k}, \epsilon) = \begin{pmatrix} H_{3 \times 3}^U(\mathbf{k}, \epsilon) & 0 \\ 0 & H_{3 \times 3}^L(\mathbf{k}, \epsilon) \end{pmatrix}, \quad (5)$$

where the upper and lower blocks of the Hamiltonian are

$$H_{3 \times 3}^U(\mathbf{k}, \epsilon) = \begin{pmatrix} F & K_t & -iH_t \\ K_t & G & \Delta - iH_t \\ iH_t & \Delta + iH_t & \lambda \end{pmatrix} \quad (6)$$

and

$$H_{3 \times 3}^L(\mathbf{k}, \epsilon) = \begin{pmatrix} F & K_t & iH_t \\ K_t & G & \Delta + iH_t \\ -iH_t & \Delta - iH_t & \lambda \end{pmatrix}. \quad (7)$$

The elements appearing in the  $3 \times 3$  Hamiltonian matrices are

$$F = \Delta_1 + \Delta_2 + \lambda + \theta \quad (8)$$

$$G = \Delta_1 - \Delta_2 + \lambda + \theta \quad (9)$$

$$K_t = \frac{\hbar^2}{2m_0} A_5 k_t^2 \quad (10)$$

$$H_t = \frac{\hbar^2}{2m_0} A_6 k_t k_z \quad (11)$$

$$\Delta = \sqrt{2} \Delta_3 \quad (12)$$

$$\lambda = \frac{\hbar^2}{2m_0} (A_1 k_z^2 + A_2 k_t^2) + D_1 \epsilon_{zz} + D_2 (\epsilon_{xx} + \epsilon_{yy}) \quad (13)$$

$$\theta = \frac{\hbar^2}{2m_0} (A_3 k_z^2 + A_4 k_t^2) + D_3 \epsilon_{zz} + D_4 (\epsilon_{xx} + \epsilon_{yy}) \quad (14)$$

Here,  $m_0$  is the free electron mass, the  $A'_i$ 's are effective mass parameters, the  $D'_i$ 's are the Bir-Pikus deformation potentials, and the  $\Delta$ 's are related to the crystal field splitting,  $\Delta_{cr}$ , and spin-orbit splitting,  $\Delta_{so}$ , by  $\Delta_1 = \Delta_{cr}$  and  $\Delta_2 = \Delta_3 = \Delta_{so}/3$ .

## B. Material parameters

The material parameters for GaN and InN are shown in Table I. Unless otherwise stated, the parameters are taken from Ref. 18.

The temperature dependent direct band gaps are given by the empirical Varshni formula<sup>24</sup>

$$E_g(T) = E_g - \frac{\alpha_g T^2}{T + \beta_g} \quad (15)$$

where  $E_g$  is the band gap at absolute zero,  $T$  is the temperature and  $\alpha_g$  and  $\beta_g$  are the Varshni parameters. These band gap parameters are listed in Table I for wurtzite GaN and InN.

For the  $\text{In}_x\text{Ga}_{1-x}\text{N}$  alloy the temperature and composition dependent band gap is given by

$$E_g(x, T) = x E_{g, \text{InN}} + (1 - x) E_{g, \text{GaN}} - bx(1 - x) \quad (16)$$

where  $E_{g, \text{InN}}$  and  $E_{g, \text{GaN}}$  are the temperature dependent band gaps in bulk InN and GaN as given in Eq. 15 and  $b = 3.0$  eV is the band gap bowing parameter for  $\text{In}_x\text{Ga}_{1-x}\text{N}$ .<sup>18</sup> While the value of the GaN band gap is well known, there is some uncertainty in the value of the InN band gap used in computing the band gap in  $\text{In}_x\text{Ga}_{1-x}\text{N}$ . The InN band gap determined from absorption measurements on InN samples range from 1.7 to 3.1 eV with most values centered around 1.9 eV.<sup>25</sup> Based on optical measurements on ultrapure InN samples, it has recently been suggested<sup>25,26,27,28</sup> that InN is a narrow gap semiconductor with a band gap of 0.7 eV as opposed to 1.994 eV as cited in Ref. 18. Nevertheless, for the small values of the Indium concentration,  $x$ , that we use in this study, the computed band gap for  $\text{In}_x\text{Ga}_{1-x}\text{N}$  should be rather insensitive to the assumed value of the InN band gap and we adopt the InN band gap and band gap bowing parameter for the  $\text{In}_x\text{Ga}_{1-x}\text{N}$  alloy cited in Ref. 18. Since the band bowing parameter,  $b$ , for  $\text{In}_x\text{Ga}_{1-x}\text{N}$  based on an InN band gap of 0.7 eV has not been redetermined,

TABLE I: Material parameters for wurtzite GaN and InN. Values are taken from Ref. 18 unless indicated otherwise.

Parameter	GaN	InN
<u>Mass Density</u>		
$\rho_0$ (gm/cm <sup>3</sup> )	6.15	6.81
<u>Lattice constants</u>		
$a_0$ (Å)	3.189	3.545
$c_0$ (Å)	5.185	5.703
<u>Direct band gaps</u>		
$E_g$ (eV)	3.507	1.994
$\alpha_g$ (meV/K)	0.909	0.245
$\beta_g$ (K)	830	624
<u>Hole splitting energies</u>		
$\Delta_{cr}$ (eV)	0.019	0.041
$\Delta_{so}$ (eV)	0.014	0.001
<u>Electron effective masses</u>		
$m_z^*$ (m <sub>0</sub> )	0.2	0.12
$m_{xy}^*$ (m <sub>0</sub> )	0.2	0.12
<u>Hole effective mass parameters</u>		
$A_1$	-6.56	-8.21
$A_2$	-0.91	-0.68
$A_3$	5.65	7.57
$A_4$	-2.83	-5.23
$A_5$	-3.13	-5.11
$A_6$	-4.86	-5.96
<u>Electron deformation potentials</u>		
$a_{c,z}$ (eV)	-6.5	-3.5
$a_{c,xy}$ (eV)	-11.8	-3.5
<u>Hole deformation potentials</u>		
$D_1$ (eV)	-3.0	-3.0
$D_2$ (eV)	3.6	3.6
$D_3$ (eV)	8.82	8.82
$D_4$ (eV)	-4.41	-4.41
<u>Elastic stiffness constants</u>		
$C_{11}$ (GPa)	390	223
$C_{12}$ (GPa)	145	115
$C_{13}$ (GPa)	106	92
$C_{33}$ (GPa)	398	224
<u>Piezoelectric constants</u>		
$e_{13}$ (C/m <sup>2</sup> )	-0.35	-0.57
$e_{33}$ (C/m <sup>2</sup> )	1.27	0.97
<u>Dielectric constants</u>		
$\epsilon_0$	8.9 <sup>a</sup>	15.3 <sup>b</sup>
$\epsilon_\infty$	5.7 <sup>c</sup>	8.4 <sup>c</sup>
<u>Refractive index</u>		
$n$	2.27 <sup>d</sup>	2.71 <sup>e</sup>

<sup>a</sup>Ref. 19.

<sup>b</sup>Ref. 20.

<sup>c</sup>Ref. 21.

<sup>d</sup>Ref. 22.

<sup>e</sup>Ref. 23.

our use of the older parameters has the virtue of including band bowing effects in our calculations for small values of  $x$ .

We obtain electron effective masses for  $\text{In}_x\text{Ga}_{1-x}\text{N}$  by linearly interpolating the reciprocals of the masses as a function of  $x$ , i.e., the concentration dependent effective masses are taken to be

$$\frac{1}{m_{xy}^*(x)} = x \left( \frac{1}{m_{xy}^*} \right)_{\text{InN}} + (1-x) \left( \frac{1}{m_{xy}^*} \right)_{\text{GaN}} \quad (17\text{a})$$

$$\frac{1}{m_z^*(x)} = x \left( \frac{1}{m_z^*} \right)_{\text{InN}} + (1-x) \left( \frac{1}{m_z^*} \right)_{\text{GaN}}. \quad (17\text{b})$$

For all other material parameters in Table I, we use linear interpolation in the composition to obtain values for the alloy.

### C. Carrier states in multi-quantum well diode

In computing the electronic states in the intrinsic region of the pin diode shown in Fig. 1, we take the barriers in the *ohmic contacts* to be infinite for simplicity. The quantum confinement potentials for electrons and holes in the intrinsic region arise from bandgap discontinuities between well and barrier regions and the strain-induced piezoelectric field. Thus the confinement potential is

$$V_\alpha(z, t) = V_{\alpha, \text{gap}}(z) + V_{\text{piezo}}(z), \quad (18)$$

where  $\alpha = \{c, v\}$  distinguishes between electrons and holes.

If the position-dependent band gap in the MQW is  $E_g(z)$  as determined from Eq. 15, then the confinement potentials for electrons and holes are given by

$$V_{c, \text{gap}}(z) = E_{g, \text{min}} + Q_c (E_g(z) - E_{g, \text{min}}) \quad (19\text{a})$$

$$V_{v, \text{gap}}(z) = -(1 - Q_c) (E_g(z) - E_{g, \text{min}}) \quad (19\text{b})$$

where  $E_{g, \text{min}} = \min_z [E_g(z)]$  is the minimum of the position dependent band gap and  $Q_c = 0.6$  is the conduction band offset.<sup>29</sup>

The confinement potential due to the strain-induced piezoelectric field satisfies

$$\frac{dV_{\text{piezo}}(z)}{dz} = |e| E_z^0(z), \quad (20)$$

where  $|e|$  is the electric charge and  $E_z^0(z)$  is the strain-induced piezoelectric field. The piezoelectric field in the diode is obtained from the requirement that the electric displacement vanishes.<sup>30</sup> Thus

$$E_z^0(z) = - \frac{4\pi}{\epsilon_0(z)} (P_z^0(z) + P_0), \quad (21)$$

where  $P_0$  is a constant polarization induced by the externally applied voltage,  $\Delta V$ , and  $\epsilon_0(z)$  is the position-dependent static dielectric constant. The value of  $P_0$

is obtained from the voltage drop across the diode (of length  $L$ ). The voltage drop in Fig. 1 between source and drain due to the induced piezoelectric field is just

$$\Delta V = - \int_0^L dz E_z^0(z), \quad (22)$$

from which  $P_0$  can be determined. The magnitude of the strain-induced polarization directed along the  $z$ -direction is given by

$$P_z^0(z) = e_{31}(z) (\epsilon_{xx}(z) + \epsilon_{yy}(z)) + e_{33}(z) \epsilon_{zz}(z), \quad (23)$$

where  $e_{31}(z)$  and  $e_{33}(z)$  are the position-dependent piezoelectric constants and  $\epsilon_{xx}(z)$ ,  $\epsilon_{yy}(z)$  and  $\epsilon_{zz}(z)$  are the position-dependent strain tensor components. The orientation of the strain-induced polarization,  $P_z^0(z)$ , is such that the piezoelectric field opposes the built-in electric field in the intrinsic region as has been discussed in several previous studies.<sup>13,31,32,33,34,35</sup>

In a pseudomorphically strained MQW diode, the GaN source and drain contacts are assumed to be unstrained while the in-plane lattice constants in the  $\text{In}_x\text{Ga}_{1-x}\text{N}$  wells and GaN barriers adjust to the lattice constant in the source and drain. For a MQW grown along the [0001] direction (the  $z$ -direction) the  $z$ -dependent strain is given by<sup>36</sup>

$$\epsilon_{xx}(z) = \epsilon_{yy}(z) = \frac{a_0 - a(z)}{a(z)}. \quad (24)$$

Here  $a_0$  is the lattice constant in the GaN source and drain and  $a(z)$  is the  $z$ -dependent lattice constant in the MQW active region. Minimizing the overall strain, we find<sup>36</sup>

$$\epsilon_{zz}(z) = - \frac{2 C_{13}(z)}{C_{33}(z)} \epsilon_{xx}(z), \quad (25)$$

where  $C_{13}(z)$  and  $C_{33}(z)$  are  $z$ -dependent elastic stiffness constants.

The diode structure breaks translational symmetry along the  $z$  direction. Thus, quantum confinement of carriers in the MQW active region gives rise to a set of two-dimensional subbands. The effective mass wavefunctions are

$$\psi_{n, \mathbf{k}}^\alpha(\mathbf{r}) = \sum_j \frac{e^{i \mathbf{k} \cdot \mathbf{r}}}{\sqrt{A}} F_{n, k, j}^\alpha(z) |\alpha, j\rangle, \quad (26)$$

where  $\alpha = \{c, v\}$  refers to conduction or valence subbands,  $n$  is the subband index,  $\mathbf{k} = (k_x, k_y, 0) = (k, \phi)$  is the two-dimensional wavevector, and  $j$  labels the spinor component. For conduction subbands, ( $\alpha=c$ )  $j = 1, 2$  while for valence subbands ( $\alpha=v$ )  $j = 1 \dots 6$ . The slowly varying envelope functions  $F_{n, k, j}^\alpha(z)$  are real and depend only on  $k = |\mathbf{k}|$ , while the rapidly-varying Bloch basis states  $|\alpha, j\rangle$  are defined in Eqs. (1) and (3). The valence Bloch basis states depend on the orientation,  $\phi$ , of  $\mathbf{k}$  in the  $xy$  plane as given in Eq. (4). The area of the MQW

sample in the  $xy$  plane is  $A$ , and  $\rho = (x, y, 0)$  is the projection of  $\mathbf{r}$  in the plane.

The envelope functions satisfy a set of effective-mass Schrödinger equations

$$\sum_{j,j'} \{ H_{j,j'}^\alpha(k) + \delta_{j,j'} [V_\alpha(z) - E_n^\alpha(k)] \} F_{n,k,j'}^\alpha(z) = 0, \quad (27)$$

subject to the boundary conditions

$$F_{n,k,j}^\alpha(z=0) = F_{n,k,j}^\alpha(z=L) = 0. \quad (28)$$

where  $V_\alpha(z)$  are the quantum confinement potentials for conduction and valence electrons defined in Eq. 18 and  $E_n^\alpha(k)$  are the energy eigenvalues for the  $n$ th conduction or valence subband. Note that in the envelope function approximation, the subband energy depends only on the magnitude  $k$  of the transverse wavevector and not on the angle  $\phi$ . The matrix operators  $H_{j,j'}^\alpha(k)$  depend on  $z$  and are obtained by making the replacement  $k_z \rightarrow -i\frac{\partial}{\partial z}$  and letting all material parameters be  $z$ -dependent operators in the matrices  $H^\alpha(k, \epsilon)$  given in Eqs. (2) and (5). To ensure the Hermitian property of the Hamiltonian, we make the operator replacements<sup>37</sup>

$$B(z) \frac{\partial^2}{\partial z^2} \rightarrow \frac{\partial}{\partial z} B(z) \frac{\partial}{\partial z}, \quad (29)$$

and

$$B(z) \frac{\partial}{\partial z} \rightarrow \frac{1}{2} \left[ B(z) \frac{\partial}{\partial z} + \frac{\partial}{\partial z} B(z) \right]. \quad (30)$$

We arrive at a set of coupled ordinary differential equations (ODE's) subject to the two-point boundary value condition of Eq. (28). These are solved for the envelope functions and subband energies. In practice, we introduce a uniform grid,  $\{z_i\}$ , along the  $z$ -direction and finite-difference the effective mass Schrödinger equations to obtain a matrix eigenvalue problem which can be solved using standard matrix eigenvalue routines. The resulting eigenvalues are the subband energies,  $E_n^\alpha(k)$ , and the corresponding eigenvectors are the envelope functions,  $F_{n,k,j}^\alpha(z_i)$ , defined on the finite difference mesh.

#### D. Carrier dynamics

In two-color time resolved differential reflectivity experiments a pump laser is used to excite electrons from the valence to the conduction subbands of the multi-quantum well. The photoexcited carriers then relax through scattering, changing the optical properties of the heterostructure in the process. We simulate these processes using Boltzmann transport equations which we solve numerically.<sup>9,38</sup> For each electron and hole subband state with energy,  $E_n^\alpha(k)$ , we have a time dependent distribution function,  $f_n^\alpha(\mathbf{k}, t)$ , which gives the probability, as a function of time, of finding a conduction or valence

electron in subband  $n$  with wave vector  $\mathbf{k}$ . The Boltzmann equation including photoexcitation of hot electron-hole pairs by the pump, the subsequent cooling of these carriers by emission of confined LO phonons, and the recombination of electron-hole pairs is

$$\frac{\partial f_n^\alpha(\mathbf{k})}{\partial t} = \sum_{n',k'} \{ f_{n'}^\alpha(\mathbf{k}') W_{\mathbf{k}',\mathbf{k}}^{n',n} [1 - f_n^\alpha(\mathbf{k})] - f_n^\alpha(\mathbf{k}) W_{\mathbf{k},\mathbf{k}'}^{n,n'} [1 - f_{n'}^\alpha(\mathbf{k}')] \} + \left[ \frac{\partial f_n^\alpha(\mathbf{k})}{\partial t} \right] \quad (31)$$

To simplify the calculations, we use an axial approximation in which the distribution functions are replaced by their angular averages in the  $x$ - $y$  plane of the multi-quantum well.<sup>9,38</sup> Thus the time dependent conduction and valence electron distribution functions,  $f_n^c(k)$  and  $f_n^v(k)$ , are functions of the magnitude of  $\mathbf{k}$ .

The first two terms on the right hand side of Eq. (31) describes the rapid cooling of hot electrons and holes by emission and absorption of confined LO phonons. Rapid LO phonon scattering is an intraband process which creates quasi-thermal electron and hole distributions at their respective band edges. The confined LO phonon scattering rate in the multi-quantum well,  $W_{\mathbf{k},\mathbf{k}'}^{n,n'}$ , given in Refs. 38 and 9, is the rate at which a conduction (or valence) electron in subband  $n$  with wave vector  $\mathbf{k}$  scatters to subband  $n'$  with wave vector  $\mathbf{k}'$ .

The last term on the right hand side of Eq. (31) consists of two terms

$$\left[ \frac{\partial f_n^\alpha(\mathbf{k})}{\partial t} \right] = \left[ \frac{\partial f_n^\alpha(\mathbf{k})}{\partial t} \right]_{pump} + \left[ \frac{\partial f_n^\alpha(\mathbf{k})}{\partial t} \right]_{relax} \quad (32)$$

and describes the change in the conduction or valence electron distribution function due to the action of the pump as well as carrier relaxation through recombination of electron-hole pairs. We assume that electron-hole pairs can recombine with a phenomenological time constant  $\tau_0$ . Expressions for the photogeneration rate can be found in Ref. 9. It is assumed that the pump laser is a Gaussian pulse with an intensity FWHM of  $\tau_p$  peaked at  $t = 0$  with a Lorentzian spectral lineshape with a FWHM of  $\gamma$ .

#### E. Optical properties

For dipole transitions between conduction and valence electronic states near the band edge, we calculate optical properties using Fermi's golden rule. The contributions to the real and imaginary parts of the dielectric function from the effective mass band edge states are given by

$$\begin{aligned} \varepsilon_1(\hbar\omega) &= \frac{8\pi e^2}{V} \sum_{n,n',\mathbf{k}} \left| \hat{\epsilon} \cdot \mathbf{d}_{n,n'}^{c,v}(\mathbf{k}) \right|^2 (f_{n'}^v(k) - f_n^c(k)) \\ &\times \frac{\Delta E_{n,n'}^{c,v}(k)}{(\Delta E_{n,n'}^{c,v}(k) + \hbar\omega) (\Delta E_{n,n'}^{c,v}(k) - \hbar\omega)} \end{aligned} \quad (33)$$

and

$$\begin{aligned} \varepsilon_2(\hbar\omega) &= \frac{4\pi^2 e^2}{V} \sum_{n,n',\mathbf{k}} \left| \hat{\epsilon} \cdot \mathbf{d}_{n,n'}^{c,v}(\mathbf{k}) \right|^2 (f_{n'}^v(k) - f_n^c(k)) \\ &\times \delta(\Delta E_{n,n'}^{c,v}(k) - \hbar\omega) \end{aligned} \quad (34)$$

where  $\Delta E_{n,n'}^{c,v}(k) = E_n^c(k) - E_{n'}^v(k)$  are the  $k$ -dependent transition energies between conduction and valence subband states,  $V = A L$  is the sample volume, and  $\hat{\epsilon}$  is the unit complex polarization vector. Expressions for the dipole matrix elements  $\mathbf{d}_{n,n'}^{c,v}(\mathbf{k})$  for dipole allowed transitions between conduction subband  $n$  and valence subband  $n'$  can be found in Ref. 11.

In Eqs. (33) and (34) the spectral lineshapes are described by Dirac delta functions. In practice we replace the delta functions with Lorentzian lineshapes having a full width at half maximum (FWHM) of  $\Gamma$ . The real and imaginary parts of the dielectric function, including lineshape broadening, can be obtained from Eqs. (33) and (34) using the operator replacements<sup>37</sup>

$$\delta(\Delta E - \hbar\omega) \rightarrow \frac{\Gamma/(2\pi)}{(\Delta E - \hbar\omega)^2 + (\Gamma/2)^2} \quad (35)$$

and

$$\frac{1}{\Delta E - \hbar\omega} \rightarrow \frac{\Delta E - \hbar\omega}{(\Delta E - \hbar\omega)^2 + (\Gamma/2)^2}. \quad (36)$$

#### F. Generation and propagation of coherent acoustic phonons

The ultrafast photogeneration of electrons and holes in the InGaN multi-quantum wells by the pump gives rise to coherent longitudinal acoustic (LA) phonons which propagate into the diode structure. Coherent acoustic phonons give rise to a macroscopic lattice displacement.<sup>3,4,5,6,7,8,11,12</sup> Since the photogenerated carrier distributions are functions of  $z$ , the transient lattice displacement  $U(z, t)$  due to photogenerated carriers is independent of  $x$  and  $y$  and is parallel to  $z$ . As discussed in Refs. 11 and 3,  $U(z, t)$  satisfies a loaded string equation. In the presence of a position dependent longitudinal acoustic sound velocity,  $C_s(z)$ , we have

$$\frac{\partial^2 U(z, t)}{\partial t^2} - \frac{\partial}{\partial z} \left( C_s^2(z) \frac{\partial U(z, t)}{\partial z} \right) = S(z, t) \quad (37)$$

where  $S(z, t)$  is a driving or loading function and depends on the photogenerated carrier distributions. The longitudinal acoustic sound velocity is given by

$$C_s(z) = \sqrt{\frac{C_{33}(z)}{\rho_0(z)}} \quad (38)$$

where  $C_{33}(z)$  and  $\rho_0(z)$  are the position dependent elastic stiffness constant and mass density.

The loaded string equation is solved subject to the initial conditions

$$U(z, t = -\infty) = \frac{\partial U(z, t = -\infty)}{\partial t} = 0. \quad (39)$$

We solve the loaded string equation numerically by finite differencing Eq. (37) inside a computational box whose left edge,  $z_L$ , is the semiconductor-air interface in the p-GaN contact and whose right edge,  $z_R$ , lies inside the n-GaN substrate (see Fig. 1). At  $z_R$  we impose absorbing boundary conditions while at  $z_L$  there are no perpendicular forces at the semiconductor-air interface. Thus we solve the initial value problem subject to the left and right boundary conditions

$$\frac{\partial U(z_L, t)}{\partial z} = 0 \quad (40a)$$

and

$$\frac{\partial U(z_R, t)}{\partial z} + \frac{1}{C_s(z_R)} \frac{\partial U(z_R, t)}{\partial t} = 0. \quad (40b)$$

Starting with the second quantized Hamiltonian for the electron-phonon interaction, a microscopic expression for the driving function was derived in Ref. 11 using the density matrix formalism (see also the erratum in Ref. 12 as well as the review article in Ref. 3). In wurzite materials such as InGaN the electron-phonon interaction contains contributions from piezoelectric and deformation potential coupling. Under typical experimental conditions the microscopic expression for the driving function can be simplified to<sup>11,12</sup>

$$S(z, t) = \sum_{\nu} S_{\nu}(z, t) \quad (41)$$

where the summation index,  $\nu$ , runs over carrier species, i.e. electrons, heavy holes, light holes and split off holes. The partial driving functions including both piezoelectric and deformation potential coupling are given by

$$S_{\nu}(z, t) = \pm \frac{1}{\rho_0} \left( a_{\nu} \frac{\partial}{\partial z} + \frac{4\pi|e| e_{33}}{\epsilon_{\infty}} \right) \rho_{\nu}(z, t) \quad (42)$$

where  $\rho_0$  is the mass density,  $e_{33}$  is the piezoelectric constant,  $\epsilon_{\infty}$  is the high frequency dielectric constant and  $\rho_{\nu}(z, t)$  is the photogenerated carrier density. The deformation potentials are  $a_{\nu}$ . For conduction electrons,  $a_{\nu} = a_{c,z}$ , for heavy and light holes,  $a_{\nu} = D_1 + D_3$ , and for crystal field split holes,  $a_{\nu} = D_1$ . We note that Eq. (42) was derived in the elastic continuum limit by Chern *et al.*<sup>3</sup> The driving function satisfies the sum rule

$$\int_{-\infty}^{\infty} dz S(z, t) = 0. \quad (43)$$

as shown in Refs. 11 and 3.

Since the photoexcited holes are predominantly a mixture of heavy and light holes, we use  $a_{\nu} = D_{13} = D_1 + D_3$

in computing hole deformation potential contributions in Eq. (41). The sum over species,  $\nu$ , then yields the total driving function

$$S(z, t) = \frac{1}{\rho_0} \left\{ a_{c,z} \frac{\partial}{\partial z} + \frac{4\pi|e|e_{33}}{\epsilon_\infty} \right\} \rho_e(z, t) - \frac{1}{\rho_0} \left\{ D_{13} \frac{\partial}{\partial z} + \frac{4\pi|e|e_{33}}{\epsilon_\infty} \right\} \rho_h(z, t), \quad (44)$$

where  $\rho_e(z, t)$  and  $\rho_h(z, t)$  are the photogenerated conduction electron and valence hole densities.

The photogenerated electron and hole densities are obtained from the envelope functions defined in Eq. (26) and the time dependent electron and hole distribution functions,  $f_n^c(k, t)$  and  $f_{n'}^v(k, t)$ , obtained from solving the coupled Boltzmann equations (31). We have

$$\rho_e(z, t) = \frac{1}{A} \sum_{n,j,\mathbf{k}} (f_n^c(k, t) - f_n^{c0}(k)) |F_{n,k,j}^c(z)|^2 \quad (45a)$$

and

$$\rho_h(z, t) = \frac{1}{A} \sum_{n',j,\mathbf{k}} (f_{n'}^v(k, t) - f_{n'}^{v0}(k)) |F_{n',k,j}^v(z)|^2. \quad (45b)$$

where  $f_n^{c0}(k)$  and  $f_{n'}^{v0}(k)$  are the initial Fermi-Dirac distribution functions for conduction and valence band electrons in subbands  $n$  and  $n'$ .

The propagating coherent phonon displacement field  $U(z, t)$  gives rise to a propagating strain with

$$\varepsilon_{zz}(z, t) = \frac{\partial U(z, t)}{\partial z} \quad (46)$$

The propagating strain field alters the optical properties of the sample which is then detected by the delayed probe pulse.

### G. Transient probe response

To compute the time dependent probe transmission and reflection coefficients we need to model the dielectric function in the diode structure shown in Fig. 1. We will denote this time and position dependent dielectric function as

$$\varepsilon(\hbar\omega, z, t) = \varepsilon_1(\hbar\omega, z, t) + i \varepsilon_2(\hbar\omega, z, t) \quad (47)$$

where  $\hbar\omega$  is the probe energy. We can solve Maxwell's equations for the time dependent probe reflection coefficient,  $R(\hbar\omega, t)$ , using the transfer matrix method of Ref. 9 as described in Ref. 37.

There are several processes which contribute to the dielectric function in the InGaN/GaN multi-quantum wells. The first contribution to the dielectric function is a Drude term due to photoexcited free carriers which gives a contribution to the dielectric function of

$$\varepsilon(\hbar\omega, z, t)_D = -\frac{(\hbar\omega_p(t))^2}{(\hbar\omega)^2} \quad (48)$$

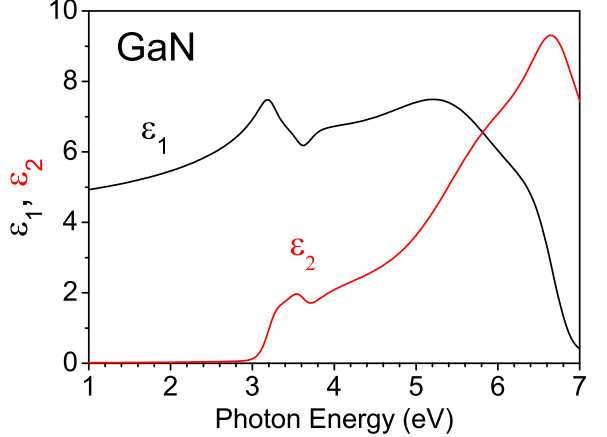


FIG. 2: (Color Online) Model dielectric function for bulk GaN at  $T = 0$  K as a function of photon energy used in calculating the dielectric function in the diode source and drain contact regions.

where  $\omega_p$  is the plasma frequency. The Drude contribution to the dielectric function in Eq. (48) is uniform in the multi-quantum well structure and vanishes everywhere else. In the random phase approximation (RPA), the time dependent plasma frequency is given by<sup>39</sup>

$$\omega_p^2(t) = \frac{4\pi e^2}{LA} \left[ \sum_{n,\mathbf{k}} \frac{f_n^c(k, t)}{m_n^*(k)} + \sum_{n',\mathbf{k}} \frac{f_{n'}^v(k, t) - 1}{m_{n'}^*(k)} \right] \quad (49)$$

where  $L = 710$  Å is the width of the multi-quantum well structure in Fig. 1 and  $A$  is the cross sectional area of the diode. The effective masses for electrons and holes are obtained from the computed energy bands as

$$\frac{1}{m_n^*(k)} = \frac{1}{\hbar^2} \frac{\partial^2 E_n^\alpha(k)}{\partial k^2}. \quad (50)$$

Note, that in our convention, the bandstructure is computed in the electron picture so that the hole masses in Eq. (50) are usually negative. Thus both terms in Eq. (49) give positive contributions to the squared plasma frequency.

Another contribution to the multi-quantum well dielectric function, which we denote  $\varepsilon(\hbar\omega, z, t)_{MQW}$ , comes from interband transition between the effective mass band edge states. The real and imaginary parts of  $\varepsilon(\hbar\omega, z, t)_{MQW}$  are given in Eqs. (33) and (34) and are time dependent due to variations in the electron and hole distribution functions with time.

There is also a background dielectric function,  $\varepsilon_b(\hbar\omega)$  due to all the higher lying electronic transitions. For simplicity, we treat these contributions to the dielectric function in the multi-quantum well region using the model dielectric function for bulk GaN in Ref. 40 with contributions from the  $E_0$  and  $E_0 + \Delta_0$  critical points

removed. These correspond to contributions from the multi-quantum well effective mass electronic states and are already included in Eqs. (33) and (34).

We assume the coherent phonon alter the background dielectric function because of strain induced variations in the energy gaps associated with each transition.<sup>41,42</sup> Density functional calculations of the deformation potentials for the  $E_1$  transitions in a number of semiconductors<sup>43</sup> have shown that the deformation potentials associated with the  $E_0$  and  $E_1$  features are equal to within 20%. Thus, at photon energies at or below the  $E_0$  and  $E_1$  transitions we assume that the effect of temperature and strain on  $\varepsilon_b$  is to introduce a *rigid shift* in the dielectric function such that

$$\varepsilon_b(\hbar\omega, z, t) = \varepsilon_b(\hbar\omega - \Delta E_g(T) - a_{cv}(\varepsilon_{xx} + \varepsilon_{yy} + \varepsilon_{zz})). \quad (51)$$

Here,  $a_{cv}$  is an effective deformation potential which we take to be  $a_{cv} = -18.3$  eV. The coherent phonon strain tensor components are,  $\varepsilon_{xx}$ ,  $\varepsilon_{yy}$ , and  $\varepsilon_{zz}$ , and  $\Delta E_g(T) = E_g(T) - E_g$  is the band gap shift due to temperature variations with  $E_g(T)$  being the temperature dependent band gap defined by the empirical Varshni formula in Eq. (15).

The total dielectric function in the multi-quantum well region is obtained by adding the Drude, multi-quantum well, and background contributions in Eqs.(48), (33), (34) and (51), i.e.

$$\varepsilon(\hbar\omega, z, t) = \varepsilon(\hbar\omega, z, t)_D + \varepsilon(\hbar\omega, z, t)_{MQW} + \varepsilon_b(\hbar\omega, z, t) \quad (52)$$

In the GaN contact regions, we use the model dielectric functions for bulk GaN described in Ref. 40. Fig. 2 shows the real and imaginary parts of the model dielectric function for bulk GaN at  $T = 0$  K in the absence of strain. Temperature and strain effects are included using the same rigid shift model as defined in Eq. (51). Note that the dielectric functions in the GaN source and drain regions are modulated by the coherent phonon strain field as it propagates through the structure.

### III. RESULTS

#### A. Multi-quantum well band structure and electronic states

The band diagram for the conduction and valence subband states in the intrinsic region of our pseudomorphically strained InGaN/GaN MQW *pin* diode structure, shown schematically in Fig. 1, can be seen in Fig. 3 as a function of position along the growth direction,  $z$ . The voltage drop across the intrinsic region of the diode is assumed to be  $\Delta V \approx 1.6$  Volts which is the experimentally measured value obtained in similar structures described in Refs. 13 and 14 for an externally applied voltage of  $V \approx 0$  Volts. The center of the MQW intrinsic region is defined to be at  $z = 0$  and the valence band potential is set to zero at this point. Since the in-plane lat-

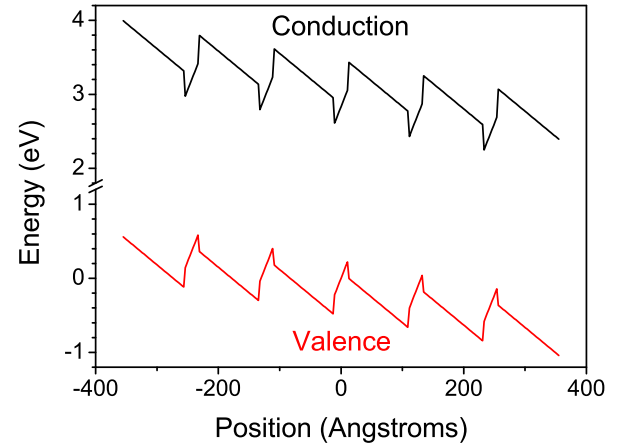


FIG. 3: (Color Online) Band diagram for conduction and valence bands in the intrinsic region of an InGaN/GaN MQW *pin* diode structure. For an external bias of  $V \approx 0$  Volts, the voltage drop across the intrinsic region of the diode is assumed to be  $\Delta V \approx 1.6$  Volts as described in the text.

tice constant throughout the structure is the same as in the GaN source and drain contacts, the GaN barriers in the MQW region are unstrained while the  $\text{In}_{0.15}\text{Ga}_{0.85}\text{N}$  wells are under biaxial compression. The electric field is 2.118 Mv/cm in the InGaN wells and -0.686 Mv/cm in the GaN barriers.

Using the confinement potentials in Fig. 3 we can solve the effective mass Schrödinger equation (27) for the electronic subbands  $E_n^\alpha(k)$  and the envelope functions,  $F_{n,k,j}^\alpha(z)$ . We can then compute the optical dipole matrix elements  $\mathbf{d}_{n,n'}^{c,v}(\mathbf{k})$ . The conduction and valence subbands,  $E_n^\alpha(k)$ , for the confinement potentials in Fig. 3 are shown in Fig. 4 as functions of  $k$  in the axial approximation. Note that the scale is different for the conduction and valance band levels in the upper and lower panels.

#### B. Multi-quantum well differential absorption

Given the conduction and valence band distribution functions  $f_n^c(k)$  and  $f_n^v(k)$ , the real and imaginary parts of the dielectric function as a function of photon energy can be obtained from Eqs. 33 and 34. The room temperature absorption coefficient in the *pin* diode MQW intrinsic region due to intersubband optical transitions between the effective mass states is shown in Fig. 5.

To illustrate the effects of carrier dynamics on the optical properties, we simulate a two-color pump-probe experiment on the diode structure with a pump laser having a photon energy of 3.2 eV ( $\lambda = 387.5$  nm) as indicated in Fig. 5. The pump fluence is assumed to be  $0.001$  J/cm<sup>2</sup> and the FWHM temporal and spectral widths are taken to be  $\tau_p = 1$  ps and  $\gamma = 4$  meV respectively. The band gap for GaN at 300 K is 3.43 eV and the band gap

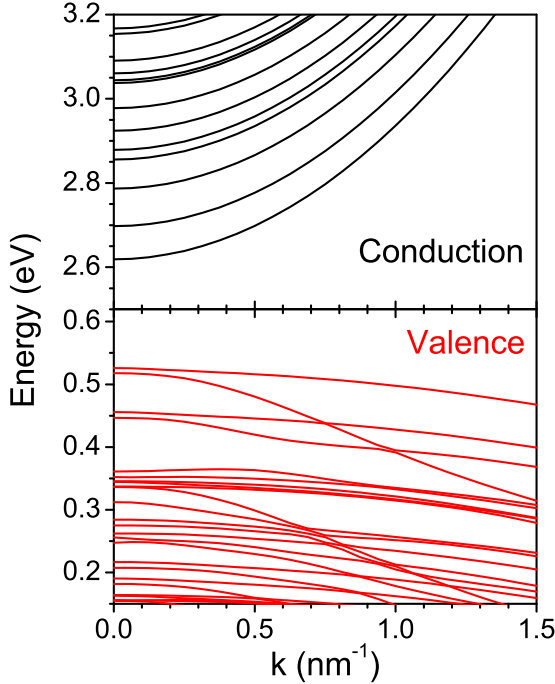


FIG. 4: (Color Online) Conduction and valence subbands for the InGaN/GaN MQW *pin* diode structure of Fig. 1 with an external bias of  $V \approx 0$  Volts.

for  $\text{In}_{0.15}\text{Ga}_{0.85}\text{N}$  is 2.87 eV. We chose the photon energy of the pump laser to lie above the band gap of the  $\text{In}_{0.15}\text{Ga}_{0.85}\text{N}$  wells but below that of the GaN barriers in order to preferentially photoexcite carriers in the wells.

The pump laser creates electron hole pairs in the quantum wells which then rapidly cool through confined optical phonon scattering and slowly recombine across the band gap. In our simulations we solve the set of Boltzmann equations in Eq. (31) for the time-dependent conduction and valence electron distribution functions  $f_n^c(k)$  and  $f_n^v(k)$ . The phenomenological electron-hole recombination time is taken to be  $\tau_0 = 100$  ps since, in an earlier experimental study,<sup>9</sup> electrons and holes in an  $\text{In}_x\text{Mn}_{1-x}\text{As}/\text{GaSb}$  heterostructure were found to recombine at midgap defects on a time scale of  $\tau_0 \approx 200$  ps. The time-dependence of the dielectric functions  $\varepsilon_1(\hbar\omega)$  and  $\varepsilon_2(\hbar\omega)$  is determined by the time-dependence of the conduction and valence band distribution functions,  $f_n^c(k)$  and  $f_n^v(k)$ .

The differential absorption coefficient, defined as the change in the absorption coefficient with respect to its initial thermal equilibrium value, is shown in Fig. 6 as a function of delay time and probe photon energy. There is a sharp dip in the differential absorption at the pump photon energy (3.2 eV) which can be attributed to *bleaching* of the direct transition between photogenerated pairs of electrons and holes. In the quantum well structure with strong built-in piezoelectric fields, a given quantum

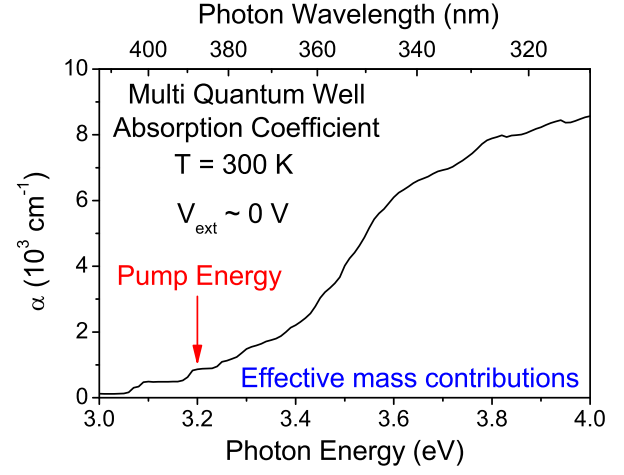


FIG. 5: (Color Online) Initial absorption coefficient at room temperature due to optical transitions between band edge effective mass states in an InGaN/GaN MQW *pin* diode structure with an external bias of  $V \approx 0$  Volts.

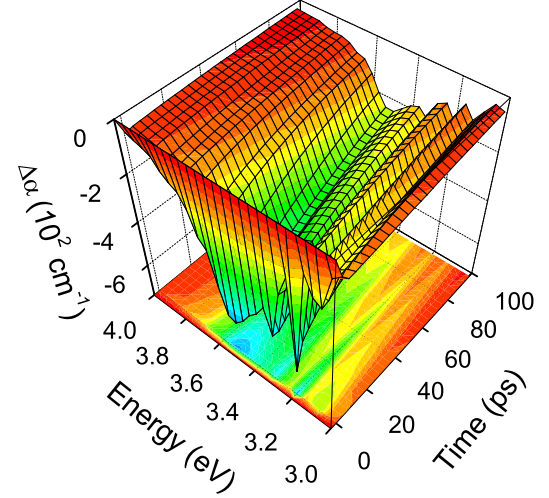


FIG. 6: (Color Online) Time dependent differential absorption as a function of delay time and probe photon energy in a simulated pump-probe experiment in a InGaN/GaN MQW *pin* diode structure with an external bias of  $V \approx 0$  Volts.

well state is optically coupled to quantum well states in adjacent wells and in the GaN continuum. When the pump creates electron-hole pairs, these interband transitions are also blocked giving rise to the negative differential absorption seen at higher photon energies in Fig. 6. The relaxation of the differential absorption as a function of delay time occurs on a time scale of hundreds of picoseconds and is controlled by intersubband recombination of the photogenerated electrons and holes.

### C. Coherent phonon generation and propagation

In our simulated pump-probe experiment, electrons and holes are photoexcited in the conduction and valence bands by the pump laser. These carriers in turn generate coherent acoustic phonons. From the photoexcited electron and hole distribution functions  $\rho_e(z, t)$  and  $\rho_h(z, t)$  defined in Eq. (45), we obtain the driving function  $S(z, t)$  from Eq. (44) and solve the coherent phonon loaded string equation numerically on a finite difference space-time grid.

The coherent phonon lattice displacement,  $U(z, t)$ , obtained from the loaded string equation (37) gives rise to a propagating strain field. The coherent phonon strain tensor component  $\varepsilon_{zz}(z, t)$  is shown in Fig. 7 as a function of position in the sample for several equally spaced delay times ranging from 0 to 100 ps.

Following photogeneration of carriers by the pump, a localized strain appears in the multi-quantum well region as can be seen in Fig. 7. This is due to near steady-state loading by the driving function at long times. Assuming the driving function,  $S(z, t)$ , is approximately time independent at long times, the loaded string equation (37) can be integrated once in the steady-state limit. The resulting steady-state strain is

$$\varepsilon_{zz}(z) = \frac{\partial U(z)}{\partial z} = - \int_{-\infty}^z dz' \frac{S(z')}{C_s^2(z')}. \quad (53)$$

where  $C_s(z')$  is the longitudinal acoustic sound speed in the InGaN quantum wells and  $S(z')$  is the approximately time independent driving function left behind in the multi-quantum well at long times. The fact that the steady-state strain is localized in the InGaN/GaN multi-quantum wells follows directly from the sum rule (43).

In addition to the localized strain in the InGaN/GaN multi-quantum well region of the diode, transient strain pulses are seen to radiate into the GaN layers at the longitudinal acoustic sound speed. Two transient strain pulses are generated, one propagating to the left and the other to the right. The leftward propagating pulse is totally reflected off the semiconductor-air interface in the p-GaN layer and trails the rightward propagating pulse as it propagates into the n-GaN layer and the GaN substrate.

### D. Differential reflectivity

The computed time resolved differential reflectivity in our simulation as a function of probe delay is shown in Fig. 8 for probe energies ranging from 3.0 to 4.0 eV in increments of 0.1 eV.

The oscillation observed in the differential reflectivity can be attributed to propagation of the strain pulse through the diode. The propagating strain tensor shown in Fig. 7 alters the local dielectric function as it propagates. The change in the complex dielectric function is

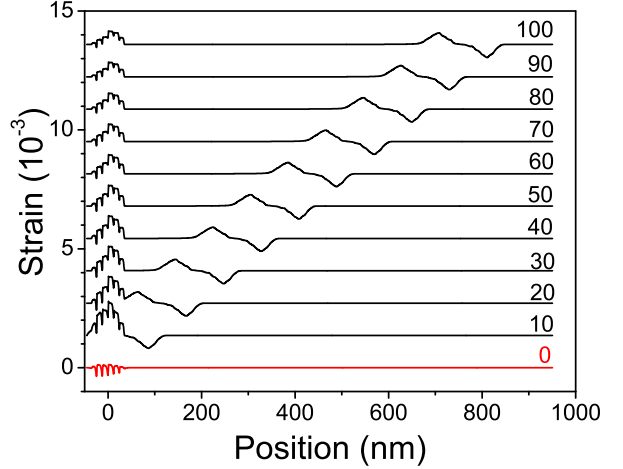


FIG. 7: (Color Online) The strain tensor component as a function of position and delay time.

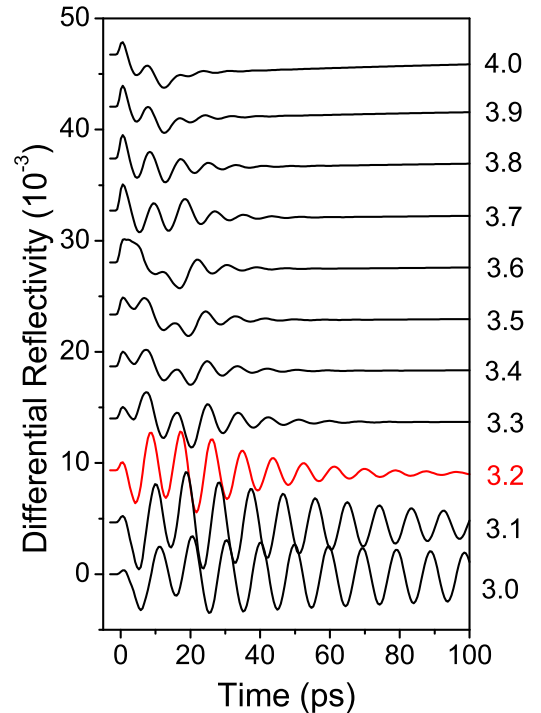


FIG. 8: (Color Online) Computed time resolved differential reflectivity as a function of probe delay for simulated pump-probe experiments on the InGaN/GaN pin diode shown in Fig. 1. The pump photon energy is 3.2 eV and differential reflectivity is computed for probe-photon energies ranging from 3.0 to 4.0 eV. The curves are offset for clarity.

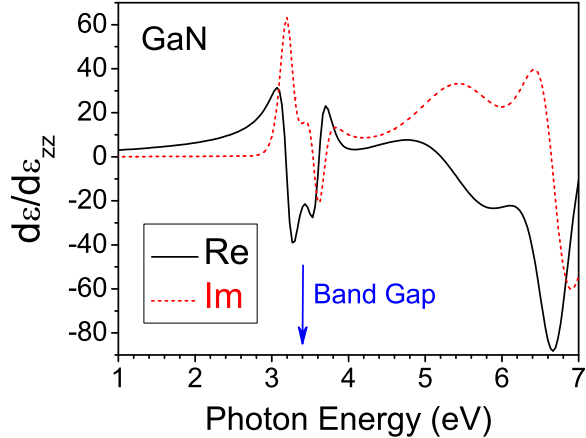


FIG. 9: (Color Online) Derivative of the complex GaN dielectric function with respect to strain as a function of the probe photon energy. The solid line is the real part and the dashed line is the imaginary part.

given by

$$\Delta\epsilon(\hbar\omega, z, t) = \frac{d\epsilon(\hbar\omega)}{d\epsilon_{zz}} \epsilon_{zz}(z, t), \quad (54)$$

The total derivative of the complex dielectric function with respect to strain in Eq. (54) measures the sensitivity of the local dielectric function to small changes in the strain induced by the coherent phonons and is obtained from the GaN model dielectric function by differentiating with respect to  $\epsilon_{zz}$  taking care to eliminate  $\epsilon_{xx}$  and  $\epsilon_{yy}$  in favor of  $\epsilon_{zz}$ . The real and imaginary parts of  $d\epsilon/d\epsilon_{zz}$  in GaN are plotted as a function of the probe photon energy in Fig. 9. The sensitivity of the dielectric function to changes in the local strain depends strongly on the probe photon energy and is especially large near the GaN band gap.

The differential reflectivity curves in Fig. 8 are obtained by solving Maxwell's equations in the structure for the dielectric function in Eq. (47). We note that the differential reflectivity signal in Fig. 8 is dominated by strong coherent phonon oscillations. In an earlier experimental and theoretical study of time resolved reflectivity in  $\text{In}_x\text{Mn}_{1-x}\text{As}/\text{GaSb}$  heterostructures (Ref. 9) we found similar oscillations in the differential reflectivity signal which were a weak perturbation on the background signal. The background signal in the earlier study was attributed to: (1) enhanced Drude absorption resulting from the increase in carriers and (2) the relaxation dynamics associated with the relaxation of highly nonequilibrium photoexcited carriers. In the time resolved differential reflectivity studies of two-color pump-probe experiments in  $\text{InMnAs}/\text{GaSb}$  heterostructures described in Ref. 9, coherent acoustic phonons were generated *exclusively* through the deformation potential electron phonon interaction.<sup>9</sup> The strong differential reflectivity oscilla-

tions seen in the present study, in contrast to the earlier one, can be attributed to an *order of magnitude enhancement* in the coherent phonon driving function,  $S(z, t)$ , due to the strong piezoelectric electron-phonon interaction term in Eq. (44).

The reflectivity oscillations can be qualitatively understood as follows. The propagating strain pulse in Fig. 7 gives rise to a perturbation in the GaN dielectric function which propagates at the acoustic sound speed. Our diode structure with the propagating perturbation in the dielectric function acts as a Fabry-Perot interferometer and the period of the reflectivity oscillations due to the propagating coherent acoustic phonon wavepacket is approximately<sup>5</sup>

$$T = \frac{\lambda}{2 C_s n(\lambda)} \quad (55)$$

where  $\lambda = 2\pi c/\omega$  is the probe wavelength,  $\hbar\omega$  is the probe photon energy,  $C_s$  is the LA sound speed in GaN and  $n(\lambda)$  is the wavelength dependent refractive index. The refractive index can be obtained from the GaN model dielectric function in Fig. 2 as<sup>44</sup>

$$n(\lambda) = \sqrt{\frac{1}{2} \left( \epsilon_1(\lambda) + \sqrt{\epsilon_1(\lambda)^2 + \epsilon_2(\lambda)^2} \right)} \quad (56)$$

The index of refraction in GaN obtained from the model dielectric function in Fig. 2 and using Eq. (56) is shown in the upper panel of Fig. 10 as a function of probe photon energy and the period of the coherent phonon induced reflectivity oscillations based on the estimate of Eq. (55) is shown as a solid line in the lower panel. The period of the reflectivity oscillations obtained from our simulations and presented in Fig. 8 are plotted in the lower panel of Fig. 10 as dots. As we can see, the simulation results agree very closely with the simple estimate in Eq. (55).

In Fig. 8, the coherent phonon induced reflectivity oscillations are observed to decay as a function of probe delay and we note that the temporal decay of the reflectivity signal is more rapid at higher probe photon energies. This has nothing to do with decay of the propagating coherent phonon strain pulse, but rather can be attributed to the fact that the absorption coefficient in GaN is rapidly increasing with probe photon energy above 3.0 eV as can be inferred from the imaginary part of the GaN model dielectric function in Fig. 2. Hence, at shorter wavelengths, the probe can not penetrate into the sample to detect the phonons.

### E. Coherent control of differential reflectivity

Coherent optical control of coherent acoustic phonon induced differential transmission oscillations by means of femtosecond laser sources has been experimentally demonstrated in  $\text{InGaN}/\text{GaN}$  multi-quantum well structures in Refs. 7 and 8. In Ref. 7 control of coherent differential transmission oscillations is achieved in a 14 period

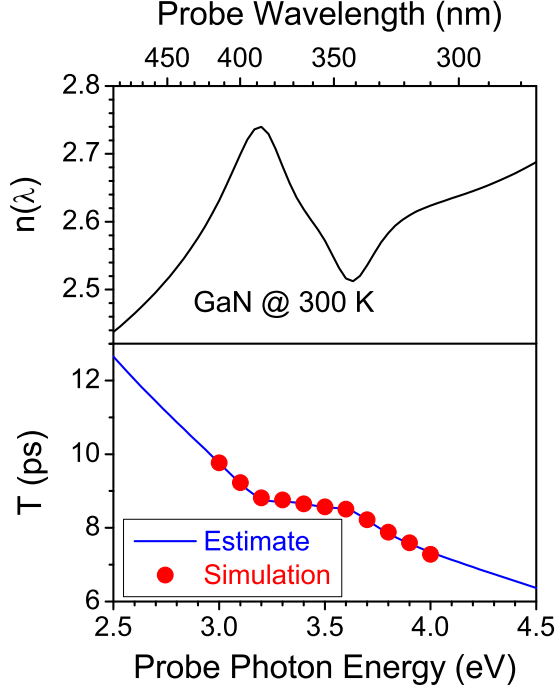


FIG. 10: (Color Online) Index of refraction in GaN (upper panel) and period of coherent phonon induced reflectivity oscillations (lower panel) as functions of probe photon energy. The solid curve in the lower panel is based on Eq. (55) while the dots are obtained from the simulations described in the text and presented in Fig. 8.

InGaN/GaN multi-quantum well sample by means of a control pulse whose time delay and intensity could be controlled independently.<sup>3,7</sup>

In this paper, we investigate the feasibility of optical control of the differential reflectivity oscillations in the *pin* diode structure shown in Fig. 1. We consider a simple control scenario in which a 3.2 eV pump pulse is followed by a delayed 3.2 eV control pulse with the same Gaussian lineshape as the pump but with possibly a different fluence.

Figs. 11 (a) and (b) illustrate how the simulated time resolved differential reflectivity signals seen in Fig. 8 can be controlled by means of a delayed control pulse for probe photon energies of 3.0 and 3.2 eV, respectively. The curves at the bottom of the figures are the time resolved differential reflectivity signals in the absence of a control pulse and are the same as the corresponding curves in Fig. 8. The upper two curves in Figs. 11 (a) and (b) are simulated transient differential reflectivity signals in a pump-probe experiment with a delayed control pump in phase and out of phase with the reflectivity oscillation period. Both initial and control pulses are 1 ps Gaussian pulses with linewidths of 4 meV and a photon energy of 3.2 eV. We varied the fluence of the control pulse relative to the initial pulse in order to maximize

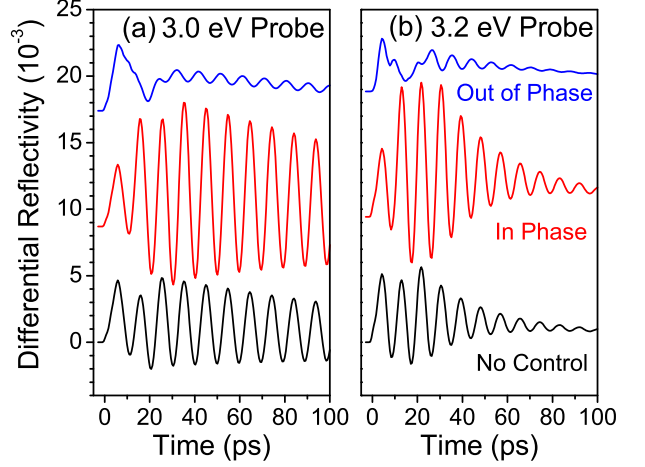


FIG. 11: (Color Online) Differential reflectivity as a function of probe delay for probe photon energies of (a) 3.0 eV and (b) 3.2 eV. The curves are offset for clarity. The pump photon energies are 3.2 eV in all cases. The lower curves show the differential reflectivity in the absence of a control pulse while the middle and upper curves are, respectively, the differential reflectivity with a 3.2 eV control pulse in phase and out of phase with the reflectivity oscillations at the probe photon energy. The best control results for destructive interference are achieved with control pulses having approximately twice the fluence of the initial pump pulse.

destructive interference in the differential reflectivity for the out of phase cases. We got the best results using a control pump having twice the fluence of the initial pump. The middle two curves in the Figs. 11 (a) and (b) show the time resolved differential reflectivity when the control pulses are in phase with the period of the reflectivity oscillations. As we can see the time resolved differential reflectivity curves in this case are enhanced due to constructive interference.

#### IV. SUMMARY AND CONCLUSIONS

In summary, we have simulated time-dependent two-color differential reflectivity experiments on a pseudomorphically strained piezoelectric InGaN/GaN multi-quantum well in a *pin* diode including both the background and oscillating coherent phonon signal. We perform simulations in which the pump laser creates electron-hole pairs in the strained InGaN wells by pumping below the GaN band gap. We conclude that very large amplitude differential reflectivity oscillations result from the generation of coherent acoustic phonon wavepackets in the multi-quantum well and their subsequent propagation into the diode. The propagation of these coherent, localized strain pulses into the diode results in a position- and frequency-dependent dielectric function which propagates at the LA phonon sound

speed. The diode with the propagating disturbance acts like a Fabry-Perot interferometer and the period of the differential reflectivity oscillations, determined from a simple geometrical optics argument, is proportional to the probe wavelength.

To take into account the time dependent background differential reflectivity, we modeled the two-color pump-probe reflectivity experiments in a Boltzmann equation formalism. Electronic structure in the InGaN/GaN multi-quantum well was calculated using  $\vec{k} \cdot \vec{p}$  theory. We included 1) photogeneration of hot carriers in the multi-quantum wells by a pump laser and 2) their subsequent cooling by emission and absorption of confined LO phonons. Nonradiative recombination of electron-hole pairs was also included in a simple relaxation time approximation. We found that the background differential reflectivity signal in our simulated diode for probe photon energies near the band gap was smaller than the

amplitude of the coherent phonon induced differential reflectivity oscillations.

We demonstrate that coherent optical control of the time resolved differential reflectivity can be achieved. We have investigated the feasibility of optically controlling the differential reflectivity signal using a delayed control pulse with the same photon energy and linewidth as the pump but with a different fluence. By applying the control pulse with a time delay in phase and out of phase with the differential reflectivity oscillations, the differential reflectivity signal can be selectively amplified or suppressed.

### Acknowledgments

This work was supported by NSF through DMR-0325474.

---

<sup>1</sup> T. Dekorsy, T. Pfeifer, W. Kutt, and H. Kurz, Phys. Rev. B **47**, 3842 (1993).

<sup>2</sup> A. V. Kuznetsov and C. J. Stanton, Phys. Rev. B **51**, 7555 (1995).

<sup>3</sup> G.-W. Chern, C.-K. Sun, G. D. Sanders, and C. J. Stanton, in *Topics in Applied Physics*, edited by K.-T. Tsen (Springer-Verlag, New York, 2004), vol. 92, pp. 339–394.

<sup>4</sup> C. J. Stanton, G. D. Sanders, R. Liu, G.-W. Chern, C.-K. Sun, J. S. Yahng, Y. D. Jho, J. Y. Sohn, E. Oh, and D. S. Kim, Superlatt. and Microstruct. **34**, 525 (2003).

<sup>5</sup> J. S. Yahng, Y. D. Jho, K. J. Yee, E. Oh, J. C. Woo, D. S. Kim, G. D. Sanders, and C. J. Stanton, Appl. Phys. Lett. **80**, 4723 (2002).

<sup>6</sup> R. Liu, C. S. Kim, G. D. Sanders, C. J. Stanton, J. S. Yahng, Y. D. Jho, K. J. Yee, E. Oh, and D. S. Kim, Phys. Rev. B **72**, 195335 (2005).

<sup>7</sup> C.-K. Sun, Y.-K. Huang, J.-C. Liang, A. Abare, and S. P. DenBaars, Appl. Phys. Lett. **78**, 1201 (2001).

<sup>8</sup> Ümit Özgür, C.-W. Lee, and H. O. Everitt, Phys. Rev. Lett. **86**, 5604 (2001).

<sup>9</sup> G. D. Sanders, C. J. Stanton, J. Wang, J. Kono, A. Oiwa, and H. Munekata, Phys. Rev. B **72**, 245302 (2005).

<sup>10</sup> J. Wang, Y. Hashimoto, J. Kono, A. Oiwa, H. Munekata, G. D. Sanders, and C. J. Stanton, Phys. Rev. B **72**, 153311 (2005).

<sup>11</sup> G. D. Sanders, C. J. Stanton, and C. S. Kim, Phys. Rev. B **64**, 235316 (2001).

<sup>12</sup> G. D. Sanders, C. J. Stanton, and C. S. Kim, Phys. Rev. B **66**, 079903 (2002).

<sup>13</sup> Y. D. Jho, J. S. Yahng, E. Oh, and D. S. Kim, Appl. Phys. Lett. **79**, 1130 (2001).

<sup>14</sup> Y. D. Jho, J. S. Yahng, E. Oh, and D. S. Kim, Phys. Rev. B **66**, 035334 (2002).

<sup>15</sup> J. B. Jeon, B. C. Lee, M. Sirenko, K. W. Kim, and M. A. Littlejohn, J. Appl. Phys. **82**, 386 (1997).

<sup>16</sup> S. L. Chuang and C. S. Chang, Phys. Rev. B **54**, 2491 (1996).

<sup>17</sup> S. L. Chuang and C. S. Chang, Appl. Phys. Lett. **68**, 1657 (1996).

<sup>18</sup> I. Vurgaftman, J. R. Meyer, and L. R. Ram-Mohan, J. Appl. Phys. **89**, 5815 (2001).

<sup>19</sup> B. Doshi, K. F. Brennan, R. Bicknell-Tassius, and F. Grunthaner, Appl. Phys. Lett. **73**, 2784 (1998).

<sup>20</sup> G. Martin, A. Botchkarev, A. Rockett, and H. Morkoç, Appl. Phys. Lett. **68**, 2541 (1996).

<sup>21</sup> F. Bernardini, V. Fiorentini, and D. Vanderbilt, Phys. Rev. Lett. **79**, 3958 (1997).

<sup>22</sup> G. Yu, G. Wang, H. Ishikawa, M. Umeno, T. Soga, T. Egawa, J. Watanabe, and T. Jimbo, Appl. Phys. Lett. **70**, 3209 (1997).

<sup>23</sup> H. F. Yang, W. Z. Shen, Z. G. Qian, Q. J. Pang, H. Ogawa, and Q. X. Guo, J. Appl. Phys. **91**, 9803 (2002).

<sup>24</sup> Y. P. Varshni, Physica **34**, 149 (1967).

<sup>25</sup> W. Walukiewicz, Physica E **20**, 300 (2004).

<sup>26</sup> V. Y. Davydov, A. A. Klochikhin, R. P. Seisyan, V. V. Emtsev, S. V. Inanov, F. Bechstedt, J. Furthmüller, H. Harima, A. V. Mudryi, J. Aderhold, et al., Phys. Stat. Solidi. (b) **229**, R1 (2002).

<sup>27</sup> J. Wu, W. Walukiewicz, K. M. Yu, J. W. A. III, E. E. Haller, H. Lu, W. J. Schaff, Y. Saito, and Y. Nanishi, Appl. Phys. Lett. **80**, 3967 (2002).

<sup>28</sup> T. Matsuoka, H. Okamoto, N. Nakao, H. Harima, and E. Kurimoto, Appl. Phys. Lett. **81**, 1246 (2004).

<sup>29</sup> S. Nakamura and G. Fasol, *The blue laser diode: GaN based emitters and lasers* (Springer-Verlag, Berlin, 1997).

<sup>30</sup> D. L. Smith and C. Mailhot, J. Appl. Phys. **63**, 2717 (1988).

<sup>31</sup> P. Lefebvre, A. Morel, M. Gallart, T. Taliercio, J. Allgre, B. Gil, H. Mathieu, B. Damilano, N. Grandjean, and J. Massies, Appl. Phys. Lett. **78**, 1252 (2001).

<sup>32</sup> T. Takeuchi, C. Wetzel, S. Yamaguchi, H. Sakai, H. Amano, I. Akasaki, Y. Kaneko, S. Nakagawa, Y. Yamamoto, and N. Yamada, Appl. Phys. Lett. **73**, 1691 (1998).

<sup>33</sup> J. S. Im, H. Kollmer, J. Off, A. Sohmer, F. Scholz, and A. Hangleiter, Phys. Rev. B **57**, R9435 (1998).

<sup>34</sup> C. Wetzel, T. Takeuchi, H. Amano, and I. Akasaki, Phys. Rev. B **61**, 2159 (2000).

<sup>35</sup> S. F. Chichibu, T. Azuhata, T. Sota, T. Mukai, and

S. Nakamura, *Appl. Phys. Lett.* **88**, 5153 (2000).

<sup>36</sup> A. F. Wright, *J. Appl. Phys.* **82**, 2833 (1997).

<sup>37</sup> S. L. Chuang, *Physics of Optoelectronic Devices* (Wiley, New York, 1995).

<sup>38</sup> G. D. Sanders and C. J. Stanton, *Phys. Rev. B* **57**, 9148 (1998).

<sup>39</sup> W. Schäfer and M. Wegener, *Semiconductor Optics and Transport Phenomena* (Springer, New York, 2002).

<sup>40</sup> A. B. Djurišić and E. H. Li, *J. Appl. Phys.* **84**, 2848 (1999).

<sup>41</sup> C. Thomsen, J. Strait, Z. Vardeny, H. J. Maris, J. Tauc, and J. J. Hauser, *Phys. Rev. Lett.* **53**, 989 (1984).

<sup>42</sup> C. Thomsen, H. T. Grahn, H. J. Maris, and J. Tauc, *Phys. Rev. B* **34**, 4129 (1986).

<sup>43</sup> D. Rönnow, N. E. Christensen, and M. Cardona, *Phys. Rev. B* **59**, 5575 (1999).

<sup>44</sup> H. Haug and S. W. Koch, *Quantum Theory of the Optical and Electronic Properties of Semiconductors* (World Scientific, New Jersey, 1993).